ACS NANO

Open Access

www.acsnano.org

Article

On-Chip Tuning of Superconductivity in Fullerides via Current-Driven Rb^+ Intercalation

Konstantin P. Shchukin,* Oliver N. Gallego Lacey, Baptiste Coquinot, Jacek Jakowski, Jingsong Huang, Patrik Staudenmayer, Yannic Falke, Ram Prakash Pandeya, and Alexander Grüneis*

Cite This: https://doi.org/10.1021/acsnano.6c02466

Read Online

ACCESS | Metrics & More | Article Recommendations | Supporting Information

ABSTRACT: An in-operando electro-intercalation method for the on-chip synthesis of alkali-metal-intercalated materials and their Raman spectroscopic and transport characterization in ultrahigh vacuum (UHV) is developed. We apply this method to synthesize fulleride superconductors via Rb^+ intercalation into a C_{60} film. During the intercalation, we monitor the stoichiometry via UHV-Raman spectroscopy and probe superconductivity via transport measurements. An increase of the superconducting transition temperature from 7.0 K to 14.5 K is observed when the stoichiometry is tuned from $Rb_{2.7}C_{60}$ to Rb_3C_{60}. In our experiment, an ionic Rb^+ flux into the host material is induced by an applied electronic current via a Butler–Volmer-type mechanism. Electro-intercalation captivates through improved stoichiometric precision, the ability to smoothly vary stoichiometry via duration of current application, and the absence of a lower limit of the volume of the host material. It represents a powerful concept for the on-chip synthesis of intercalated materials, battery research, and beyond.

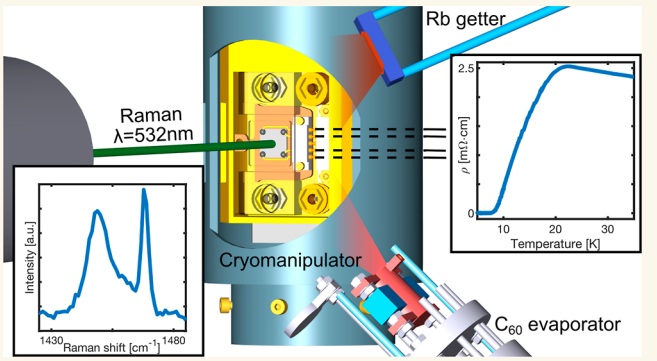

KEYWORDS: *fulleride, intercalation, alkali metal, superconductivity, Raman*

INTRODUCTION

Ionic transport is of fundamental interest in materials science and is applied in chemical functionalization of fullerenes[1] and van der Waals (vdW) materials,[2,3] iontronics,[4,5] and battery technology.[6,7] Alkali metal ion intercalation can turn fullerenes into superconductors with an A_3C_{60} stoichiometry (A = Rb, K, Cs). There is a renewed interest in superconducting fullerides for several reasons—their superconducting properties can be controlled by light,[8] C_{60} grows epitaxially on topological insulators[9] enabling superconductor-topological insulator interfaces, and the phase diagram of ternary fullerides is still poorly explored. Alkali metal intercalation into fullerenes has been achieved by intercalation from the vapor phase,[1,10−14] liquid phase,[15,16] and solid-state electrolytes.[17] Vapor-phase intercalation of alkali metal ions requires an annealing step in order to disperse the alkali metal ions throughout the sample where they occupy tetrahedral and octahedral sites in between C_{60} molecules. For example, a temperature of ∼200 °C is required for synthesizing the bulk Rb_3C_{60} phase[13,14,18] which is superconducting around 30 K.[1] Fulleride films have been studied via the van der Pauw method which was applied for vapor-phase-synthesized superconducting K_3C_{60} on Si[19] and for K_3C_{60} and Rb_3C_{60} films on the glass substrate.[20] The traditional intercalation methods have limitations and impede progress in the field toward smaller films and more precise stoichiometries. Vapor- and liquid-phase intercalations have poor control over stoichiometry, and alkali metal intercalation via a solid-state electrolyte often leads to the degradation of the electrolyte.[21] Especially, for small and thin fullerene films, tuning of the precise A_3C_{60} stoichiometry by vapor-phase intercalation is a challenge. The required annealing step is not always possible on-chip, and the intercalation from the liquid phase cannot be performed in a device configuration. Fulleride superconductivity has been explained by the large density of states from the triply degenerate lowest unoccupied molecular orbital (LUMO) combined with strong electron–phonon coupling (EPC)[22−24] to the $H_g(2)$ phonon around 440 cm^{-1}.[25] In addition, contributions to superconductivity from Jahn–Teller effects and electronic coupling mechanisms have been noted.[26,27] Recently, an in-plane covalently bonded fullerene monolayer has been synthesized via Mg intercalation.[28] In order to address the challenges related to stoichiometrically precise synthesis of fullerides and their in-operando characterization, a new experimental approach is required, which unites

Received: February 6, 2026
Revised: May 28, 2026
Accepted: May 28, 2026

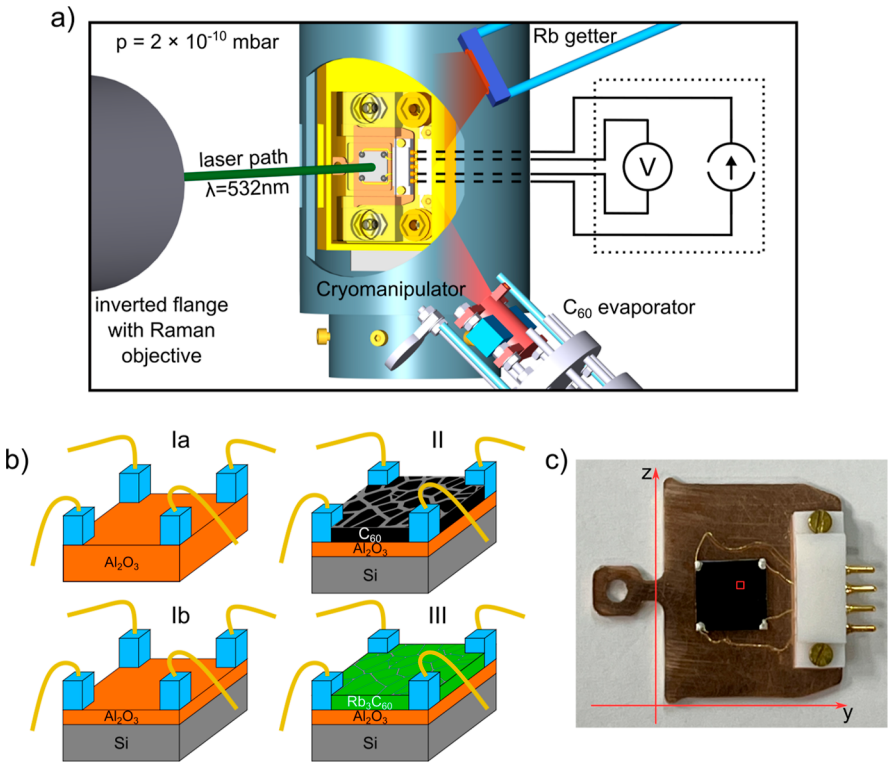

Figure 1. (a) Sketch of the setup for in-operando synthesis of Rb_xC_{60}. (b) Sample contacts and growth of Rb_3C_{60}. Ia: sapphire wafer with four contacts. Ib: 20 nm ALD-grown Al_2O_3 on Si. II: C_{60} on Al_2O_3/Si. III: Rb_3C_{60} on Al_2O_3/Si. (c) Photograph of a sample holder with the contacted sample and the four spring contacts. The red square indicates the scanning window of 0.5 mm × 0.5 mm where the Raman map in Figure 2 was recorded.

intercalation, spectroscopy, and transport measurements in a single setup.

In the present work, we perform on-chip synthesis of superconducting Rb_3C_{60} using electro-intercalation of Rb^+ into a fullerene film. We monitor the intercalation of air-sensitive Rb^+ on-chip via Raman spectroscopy and electrical transport measurements in UHV conditions.[29,30] Electro-intercalation is related to a current-driven overpotential across C_{60} grains that lowers the barrier for electron injection into the C_{60} grain. The injected electron reduces the energy required to detach and intercalate Rb^+. The resulting kinetics are well captured by a Butler–Volmer description. By the applied direct current, we fine-tune the Rb stoichiometry x in-operando and verify x via UHV-Raman spectroscopy. For a given x, we then measure the temperature-dependent resistivity $\rho(T)$ and the superconducting transition. The fingerprint $A_g(2)$ Raman mode has an energy of 1469 cm^{-1} in bulk C_{60} and 1449 cm^{-1} in bulk Rb_3C_{60},[25] allowing determination of the stoichiometry Rb_xC_{60}. We measure the intensity of C_{60} and Rb_3C_{60} modes during application of an electronic current to prove the Rb^+ intercalation.

RESULTS AND DISCUSSION

In-Operando Rb Intercalation and Sample Characterization

Figure 1a depicts the sketch of the experimental setup[30] with the sample plate with four contacts mounted on a cryomanipulator, an inverted flange with a long working distance optical objective (NA = 0.55), the Rb getter source (SAES), and the C_{60} evaporator inside a UHV chamber. The cryomanipulator is mounted on a stage with encoded motors so that Raman mapping can be performed in UHV. Figure 1b shows the substrates that have been used in this study: (1) Al_2O_3 wafers and (2) silicon wafers with a 20 nm thick Al_2O_3 film grown by Atomic Layer Deposition (ALD) as shown in Figure 1b (Ia and Ib). Using UHV-compatible conductive silver epoxy, the substrate corners were contacted via 20 μm Au wires to the spring-loaded contact pins. Upon insertion of the sample plate into the cryomanipulator, all pins are electrically connected to the nanovoltmeter and precision current source outside UHV. This setup allows us to transfer the sample out from the cryomanipulator into a heater stage for in situ annealing (not shown). After loading the electrically contacted sample plate into the cryomanipulator, we performed evaporation of 12 monolayers (MLs) of C_{60} onto the sapphire (Figure 1b II) followed by Rb evaporation (Figure 1b III). This entire process is monitored real-time by UHV-Raman spectroscopy and resistivity measurements enabling precise doping control. Figure 1c shows a photograph of the Omicron-type sample plate with four spring-loaded pin contacts attached to the sample in van der Pauw geometry.[31] The backside of the sample is attached to the sample holder using a droplet of the same UHV-compatible conductive silver epoxy. This floating configuration prevents any electrical shortening of the sample surface toward the holder during or after Rb deposition. In order to determine the location of the laser spot on the sample, we measured the distances relative to the four contacts which we identified by collecting the reflected light in a camera (Figure S1).

The UHV-Raman spectrum of the C_{60} film on sapphire is shown in Figure 2a along with a typical spectrum of a Rb-doped film with $Rb_{2.85}C_{60}$ stoichiometry in the range 1430–

https://doi.org/10.1021/acsnano.6c02466
ACS Nano XXXX, XXX, XXX–XXX

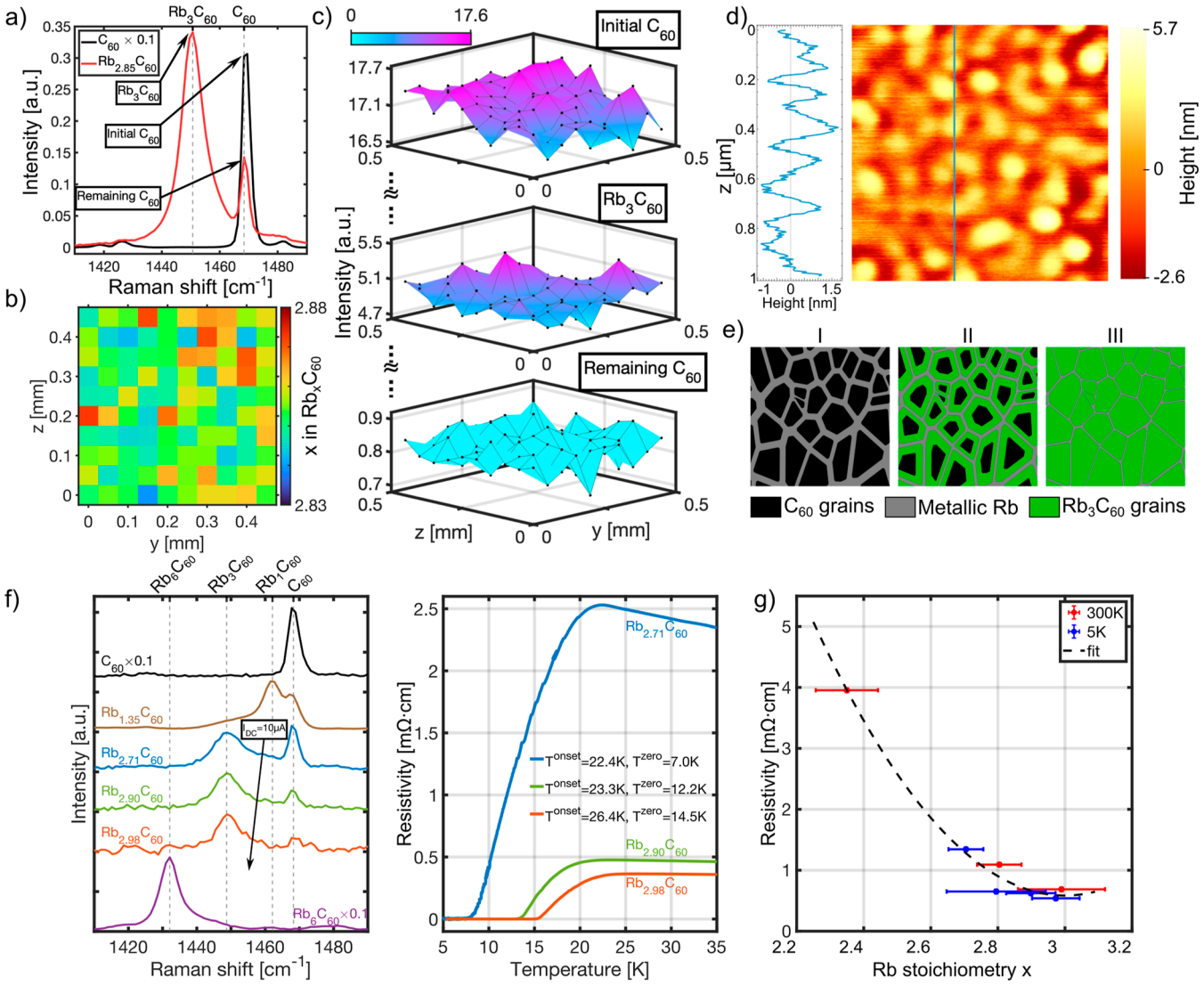

Figure 2. (a) Integrated Raman spectrum of $Rb_{2.85}C_{60}$ from the maps shown in (b) and (c). (b) Raman map of the stoichiometry x and (c) corresponding Raman maps of the initial $A_g(2)$ C_{60} peak and two $A_g(2)$ peaks of Rb_3C_{60} and remaining C_{60}. (d) Atomic force microscopy image of a 15 nm thick C_{60} film on Al_2O_3 scanned in window 1 μm × 1 μm. (e) Sketches of C_{60} grains (I) and partially (II) and fully (III) intercalated C_{60} grains with small amounts of Rb left in between the grains. (f) Raman spectra of Rb_xC_{60} and resistivity ρ characterization. 10 μA current was used to intercalate Rb. (g) ρ versus stoichiometry at T = 300 K. All Raman and transport measurements were carried out in ultrahigh vacuum.

1470 cm^{-1} which corresponds to the most intense $A_g(2)$ phonon mode. This sample was synthesized via evaporation of Rb onto the C_{60} film in UHV at 300 K. The UHV-Raman spectra were recorded at T = 5 K. This temperature was independently verified by measuring the superconducting transition of a Nb film.[30] Due to its large Raman cross section, the spectra of several MLs of doped and undoped C_{60} can be efficiently measured with a large signal/noise ratio. The Raman spectrum of the alkali metal-doped fullerene molecule depends on its charge state and has distinct frequencies for the observed phases: neutral, x = 1, x = 3, and x = 6.[25,32] For a neutral phase, it is a single peak at 1470 cm^{-1}, Rb_1C_{60} has a peak at 1458 cm^{-1}, Rb_3C_{60} at 1449 cm^{-1}, and Rb_6C_{60} at 1432 cm^{-1}. For a mixed phase, several of these peaks appear simultaneously. After determining the relative Raman cross sections for each phase, we used Raman spectroscopy to determine the stoichiometry x of a sample with an arbitrary stoichiometry and Raman components from C_{60}, Rb_1C_{60}, and Rb_3C_{60} (see Methods and Figure S2). This procedure was used for the determination of x of the sample shown in Figure 2a and yields x = 2.85. Doping homogeneity is confirmed by Raman mapping of the $A_g(2)$ peaks inside the energy window shown in Figure 2a (see Figure S3 for individual scans). The small red square in Figure 1c indicates the extent of the spatial map. Figure 2b shows a Raman map of the stoichiometry x in Rb_xC_{60} from a Raman line shape analysis yielding a spatial average of the stoichiometry of x = 2.85. Figure 2c shows Raman maps of the peak areas from the line shape analysis for the $A_g(2)$ peak of the initial pristine C_{60}, the $A_g(2)$ peak corresponding to Rb_3C_{60}, and the peak of pure C_{60} that remains after evaporation of Rb (indicated as remaining C_{60}). The Raman maps demonstrate high lateral homogeneity of both pristine and doped films, with relative standard deviations of the fitted peak areas in a range between 1.3 and 4.8%.

The sample morphology of our C_{60} films was probed by atomic force microscopy (AFM). A typical AFM image of the C_{60} film on a sapphire is shown in Figure 2d. The AFM confirms the nanostructured nature of the film reported in

https://doi.org/10.1021/acsnano.6c02466
ACS Nano XXXX, XXX, XXX−XXX

previous measurements[19,33] of K_3C_{60} and AFM measurements of C_{60}.[34] AFM analysis reveals that the 15 nm thick film consists of C_{60} grains with a lateral correlation length of 49 nm and an average roughness of 0.693 nm. The results of the AFM analysis are used in the modeling of the Rb^+ intercalation described later. The nanostructured nature is crucial for Rb intercalation because it provides a large effective surface,[35] according to which the Rb intercalation is progressing from the outside of the grain toward the inside. Hence, a partially intercalated C_{60} grain has a C_{60} core and an outer Rb_xC_{60} shell separated by a moving intercalation front. The progressive Rb intercalation into C_{60} grains is shown in Figure 2e. The excess Rb that is not intercalated into a grain forms a network of conducting channels that run in between C_{60} grains. Because of the relatively poor electrical conductivity of the network of Rb channels, a significant voltage drop can appear across the film. This situation is reminiscent of a metallic wire network across which large voltage drops have been observed.[36] The voltage drop across the sample is important for the intercalation mechanism, as described later.

We now discuss Raman and electrical transport measurements of in situ synthesized Rb_xC_{60}. Figure 2f depicts UHV-Raman spectra for sample stoichiometries between undoped ($x = 0$) and fully doped ($x = 6$) fullerides. For stoichiometries in the range $x = 3$, fullerides were metallic, and $\rho(T)$ was recorded in addition to Raman. For metallic fullerides, we can determine x from Raman and correlate it with an $\rho(T)$ trace and the appearance of superconductivity. In Figure 2f, we synthesized the phases $Rb_{1.35}C_{60}$ and $Rb_{2.71}C_{60}$ conventionally by two consecutive steps of Rb evaporation and annealing. In order to precisely control the stoichiometry for x beyond $x = 2.71$, we performed electro-intercalation of Rb^+ by passing a 10 μA current through the sample for ~96 h at $T = 300$ K which allowed for precise control of the stoichiometry. The electro-intercalation experiment was performed with the identical setup used for the van der Pauw measurements. For electro-intercalation, the applied current was ten times larger than for resistance measurements. In order to supply the Rb, electro-intercalation was performed during the deposition of ~170 MLs of Rb. We also performed electro-intercalation without Rb evaporation onto the C_{60} film. In this case, an excess amount of Rb was made available by deposition prior to the electro-intercalation. This deposited Rb acts as a reservoir from which Rb for electro-intercalation was supplied (see the next section). The electro-intercalation shown in Figure 2f was stopped at $x = 2.90$ and at $x = 2.98$ after which the sample was cooled down to $T = 5$ K. Hereafter, a Raman spectrum and a $\rho(T)$ trace (right panel of Figure 2f) were recorded. The Raman fits of stoichiometries of Figure 2f are shown in the Supporting Information (Figure S4). Both the Raman spectra and $\rho(T)$ confirm Rb^+ intercalation and the increase in stoichiometry x. Our experiments reveal that electro-intercalation at room temperature is a slow process with a rate of stoichiometry change $\Delta x = 3 \times 10^{-4}$ per 1 h. The rate of stoichiometry change corresponds to an advance of the intercalation front by a distance of 0.83 pm per hour. Hence, stoichiometry tuning is enabled by this method with a high precision that cannot be achieved by other intercalation methods. The $\rho(T)$ for the three stoichiometries ($x = 2.71$, 2.90, and 2.98) showed vanishing resistance at low temperatures which is consistent with previous reports.[19,33] This indicates that samples prepared by electro-intercalation have consistent superconducting behavior compared to samples intercalated by other methods. The stoichiometry of the samples was independently determined by UHV-Raman. This allows us to establish a precise relation between stoichiometry and $\rho(T)$, in particular the T at which ρ vanishes. We estimate the transition temperatures from the onset of vanishing resistance (T^{onset}) and the vanishing resistance (T^{zero}). T^{onset} is the temperature of the local resistivity maximum and T^{zero} is the temperature, at which the $d\rho(T)/dT < 5 \times 10^{-4}$ mΩ·cm K^{-1} in the temperature window shown in Figure 2f. We find that T^{onset} is weakly dependent on x, while T^{zero} has a strong x dependence. We rationalize this in terms of the Aslamazov–Larkin (AL) model[37] and Berezinskii–Kosterlitz–Thouless (BKT) fluctuations.[38,39] The AL model was previously used to describe the excess conductivity of K_3C_{60}[19] and the temperature regime above the critical temperature. We associate this regime with the region around the local maximum in $\rho(T)$, in which $\rho(T)$ depends on the sample dimensionality. The BKT fluctuations between temperatures T^{zero} and the critical temperature are sensitive to defects due to the incomplete stoichiometry for $x \neq 3$ and may explain the large x dependence of T^{zero}. In the present experiment, the superconducting transition broadens due to BKT fluctuations, which can be enhanced in thin films by disorder, inhomogeneity in the stoichiometry, Coulomb interactions, and surface scattering in systems with reduced dimensionality. Since the transition width also indicates the defect density, it helps to assess how far the stoichiometry is away from the optimal Rb_3C_{60}. In the present data, we observe the largest broadening for $Rb_{2.71}C_{60}$ and the sharpest transition for $Rb_{2.98}C_{60}$ in agreement to what is expected from BKT theory. We investigated Rb_3C_{60} films of 12 and 30 nm thickness (Figure S5) and found that normal-state and the superconducting response show a clear thickness dependence, consistent with bulk transport. Figure 2g depicts $\rho(x)$ at $T = 300$ K for stoichiometries x in between $x = 2.2$ and $x = 3$ with Rb_3C_{60} at the resistance minimum.[40] There is also a residual conduction of electricity through the Rb network in between the grains. The residual conduction acts as a current path in parallel to the conduction through the doped C_{60} film. The resistance minimum is not affected by the parallel channel because the resistance of the Rb network is almost ten times higher than the resistance of the doped C_{60} film (see Figure S6). The Raman spectra and $\rho(T)$ for each data point in Figure 2g are shown in the Supporting Information (Figure S7).

Current-Driven Electro-Intercalation: Experiment and Theory

Experimental Observation of Rb^+ Intercalation. In order to explain the mechanism of electro-intercalation of Rb^+ into C_{60}, we performed additional experiments with intermittent DC, continuous AC, and continuous DC currents applied to a C_{60} film with excess Rb evaporated onto its surface. During electro-intercalation, we also monitored the voltage drop across the sample and determined $\rho(t)$. Compared to dedicated measurements of the resistivity shown in Figure 2, where a current of 1 μA was applied, the $\rho(t)$ data shown here was recorded using a current of 10 μA. The larger current which is dissipated onto a partially intercalated sample and the fact that no compensation of thermoelectric voltages could be performed leads to a higher noise level. Yet, the observed time-dependent trends in ρ are unaffected by the magnitude of the current used which is

https://doi.org/10.1021/acsnano.6c02466
ACS Nano XXXX, XXX, XXX−XXX

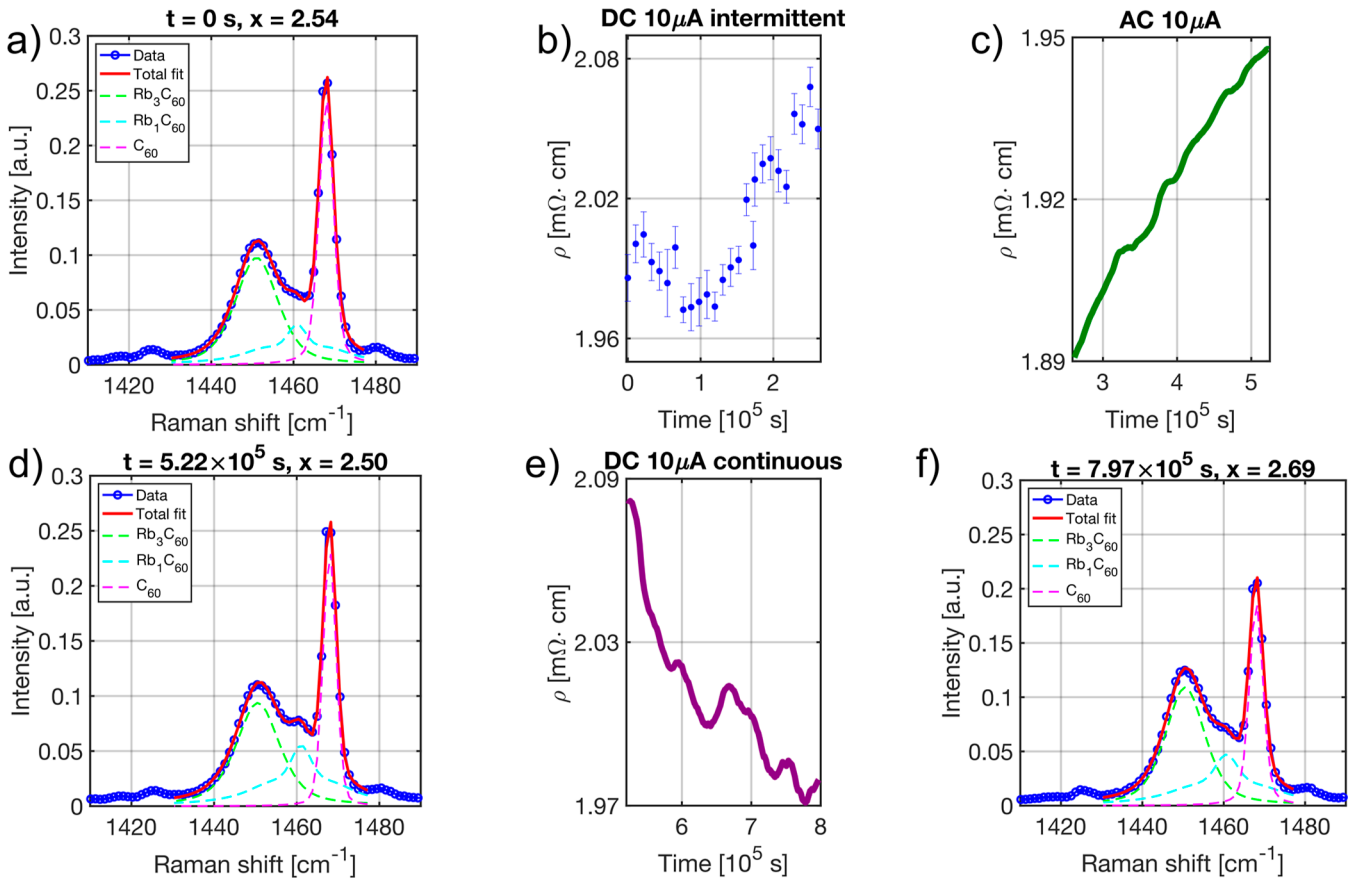

Figure 3. (a) Raman spectrum at $t = 0$ with $Rb_{2.54}C_{60}$ stoichiometry. (b,c) Time-dependent resistivity $\rho(t)$ during intermittent DC current (each 3 h for 10 s) and during AC current (1 Hz). (d) Raman spectrum at $t = 5.22 \times 10^5$ s ($Rb_{2.50}C_{60}$). (e) $\rho(t)$ during continuous DC current. (f) Raman spectra at $t = 7.97 \times 10^5$ s with stoichiometry $Rb_{2.69}C_{60}$. The AC and continuous-DC resistivity traces were smoothed using a moving-median filter with an effective time window of 2×10^4 s and a second-order Savitzky–Golay filter.

Table 1. Processes That Describe the Intercalation of Rb^+ into C_{60}[a]

process no	process description	process parameter	energy barrier E	kinetic role
I	Rb intercalation through the vdW gap between the Rb shell and C_{60}	Rb–C_{60} distance	$E = 0$ (vdW distance) $E \approx 200$ meV (10 Å)	not rate-limiting
II	diffusion of Rb inside the C_{60} grain and on its surface, leading to Rb intercalation of C_{60}	diffusion coefficient D of Rb inside C_{60}	$E \approx 200$ meV[b]	not rate-limiting
III	tunneling of an electron followed by Rb^+ intercalation described by Butler–Volmer kinetics	electron tunneling barrier between Rb and Rb_3C_{60}	$E \approx 400$ meV	rate-limiting and voltage controlled

[a]Processes I and II describe the intercalation from the vdW Gap and the Rb^+ diffusion. Process III is the tunneling of an electron followed by the Rb^+ drift and is controlled via the applied voltage and rate-limiting. [b]Estimated for the Rb-poor case.

corroborated by evaluating Raman spectra before and after current application.

Figure 3a shows the Raman spectrum collected before starting the electro-intercalation (at time $t = 0$). From this Raman spectrum, we evaluate the initial stoichiometry as $x = 2.54$. The presence of a Rb_3C_{60} peak confirms that a fraction of the deposited Rb has already intercalated. Figure 3b depicts $\rho(t)$ measured during an electro-intercalation experiment applying an intermittent 10 μA current for 10 s with a period of 3 h in between two consecutive steps of current application. Figure 3c depicts the AC electro-intercalation experiment at a frequency of 1 Hz. We observe an increase in $\rho(t)$ during the intercalation, indicating that no Rb^+ is intercalated into the C_{60} grains. The Raman spectrum (Figure 3d) taken immediately after AC electro-intercalation attempt confirms a slight reduction of Rb doping of the sample stoichiometry to $x = 2.50$. We rationalize this observation via a slow deintercalation rate which is independent of an applied current. The next experiment investigates intercalation under continuous DC application (Figure 3e). Here, $\rho(t)$ shows a decrease over time, suggesting the Rb^+ intercalation into C_{60} grains. The Raman analysis shown in Figure 3f confirms Rb intercalation by showing a clear change in stoichiometry from $x = 2.50$ to $x = 2.69$ within 2.6×10^5 s application of a 10 μA DC. This experiment confirms our earlier data of Figure 2f that the application of a 10 μA current indeed intercalates Rb to C_{60} grains and can be used as a means to fine-tune Rb_xC_{60} stoichiometry at room temperature. We now estimate what fraction of the 10 μA current is ionic. The ionic current required to explain the stoichiometry change $\Delta x \approx 0.2$ in $\Delta t \approx 2.5 \times 10^5$ s (Figure 3d,f) for the intercalation of $N_{C_{60}} \sim 5 \times 10^{14}$

https://doi.org/10.1021/acsnano.6c02466
ACS Nano XXXX, XXX, XXX–XXX

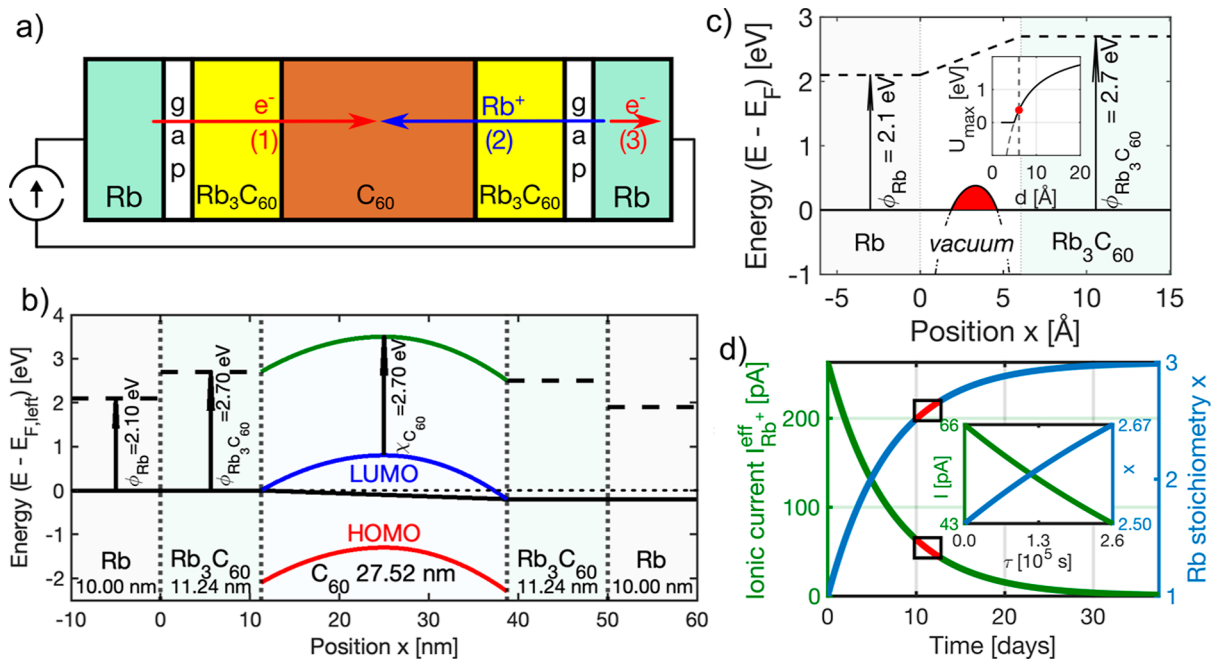

Figure 4. (a) Electro-intercalation of Rb^+ from outside the vdW distance. Sketch of cross section across a core−shell structure (Rb outside, Rb_3C_{60} inside). Electron tunneling and Rb^+ motion are indicated. (b) Band diagram of a $Rb/Rb_3C_{60}/C_{60}/Rb_3C_{60}/Rb$ heterostructure. Electron tunneling through the gaps occurs along the direction of increasing x. (c) Calculated effective tunneling barrier between Rb and Rb_3C_{60}. The inset denotes the barrier height versus the $Rb-Rb_3C_{60}$ separation. Details of the calculations are provided in Figure S10 of the Supporting Information. (d) Calculated ionic current according to the Butler−Volmer model along with the stoichiometry change (right vertical axis). Rectangles indicate the time span probed experimentally. The inset shows the experimentally relevant stoichiometry change versus time.

fullerene molecules is $I_{Rb^+} = e\frac{\Delta x}{\Delta t}N_{C_{60}} \approx 60$ pA (see Supporting Information). This is 5 orders of magnitude lower than the current of 10 μA which was used in the experiment. We thus conclude that the current is mainly electronic.

Theoretical Description of Rb^+ Electro-Intercalation. We explain the observed electro-intercalation of Rb by three essential processes that describe the intercalation of Rb across the vdW gap to a C_{60} grain (process I), the Rb^+ diffusion inside a grain of C_{60} and on its surface (process II), and the current-driven Rb^+ intercalation into C_{60} grains (process III). Process I dominates until the easily accessible Rb has been used up, and process II is very fast but depends on available Rb. The rate-limiting process III is controlled via the applied current and described by the Butler−Volmer model. Processes I−III are summarized and described in Table 1.

Process I explains why a fraction of deposited Rb intercalates spontaneously into C_{60} after Rb deposition. If Rb is within the vdW distance to C_{60} (i.e., 4.7 Å), the Rb can intercalate without having to overcome an energy barrier. We have performed calculations of the barriers for Rb intercalation into a C_{60} film with the climbing image-nudged elastic band method (CI-NEB) at three distances: the vdW distance, 10 Å, and 20 Å. For the vdW distance, the intercalation process has no barrier, i.e., it is spontaneous. The barriers for 10 Å and 20 Å are 0.24 and 0.92 eV, respectively (Figure S8). Bader charge analysis along the reaction path shows that the migrating Rb atom is neutral on the left side of the transition state where the driving force arises mainly from the cohesive energy of the Rb slab. It is clear that spontaneous Rb migration will reduce with increasing vdW gap size as all the easily available Rb is used up.

Process II describes diffusion of Rb^+ on the surface of a C_{60} grain and inside a C_{60} grain. In our calculation, we consider a Rb-poor case where one Rb^+ is intercalated in an otherwise empty C_{60} lattice and a Rb-rich case where a single Rb vacancy in Rb_3C_{60} is introduced. The Rb occupies tetrahedral centers of T_d point group symmetry (denoted as T_d) and octahedral sites of O_h point group symmetry (denoted as O_h). Our results indicate effective Rb transport via a repeating $O_h \rightarrow T_d \rightarrow O_h$ sequence along symmetry-equivalent directions which is more effective than transport via $O_h \rightarrow O_h$ and $T_d \rightarrow T_d$ hopping. The calculated energy barrier for the $T_d \rightarrow O_h$ hop of Rb is ~0.19 eV for the Rb-poor case and ~0.49 eV for a vacancy hop for the Rb-rich case (see Figure S9). The energy of the O_h site is about 0.05 eV higher than the T_d site. For the energy barrier in the Rb-rich case, we obtain a diffusion constant $D \approx 4 \times 10^{-15}$ m^2/s at 300 K. The diffusion time is estimated as $t = L^2/(2dD)$ with dimensionality $d = 1$ for thickness-limited diffusion and a film thickness $L = 15$ nm as $t \approx 10^{-2}$ s. Hence, t is negligible compared to the observed time scales for the intercalation. Processes I and II provide fast local equilibration of available Rb^+ within and around individual grains. However, this easily available Rb is generally not sufficient to synthesize Rb_3C_{60}. As we will show in the following, an applied bias is required to reach Rb_3C_{60} stoichiometry.

In process III, the intercalation of Rb^+ into a C_{60} grain proceeds via the Butler−Volmer mechanism in the presence of an applied current. This process is rate-limiting and sets the multiday time scale of the experiment. If a current is applied to a network of connected C_{60} grains surrounded by Rb, there is a voltage drop across each C_{60} grain. This is similar to metal nanowire networks where a large voltage drop inside the film of interconnected nanowires has been observed.[36] Due to the voltage drop, the barrier for electron tunneling from the Rb metal shell into the C_{60} grain is reduced. An electron that has tunneled into the C_{60} grain can attract a Rb^+ ion. In the following, we estimate the tunneling barrier. The cross section

https://doi.org/10.1021/acsnano.6c02466
ACS Nano XXXX, XXX, XXX−XXX

of the heterostructure is $Rb/Rb_3C_{60}/C_{60}/Rb_3C_{60}/Rb$. Process III involves three subprocesses 1−3 that are depicted in detail in Figure 4a. The first subprocess is an electron tunneling from the Rb metal on the left contact into the center of the C_{60} grain. The second subprocess is a Rb^+ ion being attracted by Coulomb force from the surrounding Rb to the C_{60} grain. Due to the presence of an electron inside the C_{60} core, the Rb^+ ion that detaches from the Rb metal on the right side has to overcome only a small van der Waals barrier.[41] The third subprocess is that an electron flows from the right contact to the voltage source and closes the circuit. Let us consider the tunneling subprocess 1 in more detail. The tunneling gap between the Rb metal and the Rb_3C_{60} grain is indicated in Figure 4a. In Figure 4b, we consider the band diagram across a partially intercalated C_{60} grain of total stoichiometry $x = 2.50$. The band diagram was constructed based on the literature values of electron affinity of C_{60}, $\chi_{C_{60}} = 2.7$ eV,[42] the work function of Rb, $\phi_{Rb} = 2.1$ eV,[43] the work function of Rb_3C_{60} is taken as $\phi_{Rb_3C_{60}} = 2.7$ eV, the HOMO−LUMO gap of C_{60} is taken to be $E_g = 2.3$ eV,[44] and the Fermi level of C_{60} is located 0.9 eV below the LUMO, giving a work function $\phi_{C_{60}} = \chi_{C_{60}} + 0.9 = 3.6$ eV.[45] In order to evaluate the band bending of C_{60} at the interface to Rb_3C_{60}, we consider the Fermi levels of isolated C_{60} and Rb_3C_{60} with a common vacuum level. The Fermi level of Rb_3C_{60} lies at higher energy than the Fermi level of C_{60} and electrons flow from Rb_3C_{60} to C_{60}. In the present system of a partially intercalated grain, there is a common Fermi level across the interface between the Rb_3C_{60} shell and the C_{60} core. Hence, when electrons are transferred from Rb_3C_{60} to C_{60}, the bands of C_{60} bend downward close to the interface. In Figure 4b, the band bending can be seen. The voltage drop is chosen such that the left contact is at negative potential w.r.t. the right contact.

Figure 4c depicts the effective tunneling barrier for the electron tunneling between two quantum wells resembling the Rb metal and Rb_3C_{60} with a vacuum gap in between (see Figure S10 of the Supporting Information). For the calculation of the tunneling barrier, we considered the Volta potential and effect of image charges. The Rb metal and Rb_3C_{60} are modeled as quantum wells, and bringing them closer together results in a reduction of the tunneling barrier that the electron needs to overcome when tunneling from the Rb metal into Rb_3C_{60}. For a distance of 6.06 Å, we calculated an effective barrier height equal to ~0.4 eV. The inset of Figure 4c shows the barrier as a function of Rb−Rb_3C_{60} distance. Let us now calculate the ionic Rb^+ current using the Butler−Volmer model. This model provides the interfacial ionic current density $j(\eta) = e\Gamma_s[k_f(\eta) - k_b(\eta)]$, where k_f, k_b are forward/backward rate constants, Γ_s is the effective number of sites on the C_{60} surface (here the surface density of C_{60} $\Gamma_s \approx 2/nm^2$), η is the overpotential, and e is the elementary charge. Denoting $l = 50$ nm the typical size of the grains of C_{60} and ΔV the total voltage drop, we estimate $\eta = (l/L)\Delta V \ll k_BT/e$. Using transition-state theory (TST) with transmission factor $\kappa \approx 1$ for a small overpotential η, we get the interfacial ionic current by unit of the Rb/Rb_3C_{60} interface, which we model as a section of the device for each layer of grains, that is, $wL \times L/l$. The total current in the Butler−Volmer model reads

$$I_{Rb^+} \approx \frac{\kappa w L \Gamma_s e^2 \Delta V}{2\pi\hbar} \exp\left(-\frac{\Delta G_0^{\ddagger}}{k_BT}\right) \exp(-2\kappa_{tun} d) \quad (1)$$

Here, $\Delta G_0^{\ddagger}$ is the energy barrier which corresponds to the energy required for promoting the electron into the top of the C_{60} LUMO. The last term is a tunneling rate of the electron throughout the gap of length d with transmission of $\kappa = \sqrt{2mU}/\hbar$, where U is the effective barrier and m is the free electron mass. In order to make eq 1 time-dependent, we model the effective number of C_{60} sites with a phenomenological Avrami model. This model is generally applicable for all the A_xC_{60} material system.[35] Using a current I_{Rb^+} that does not depend on the grain size, we can extract an effective ionic current:

$$I_{Rb^+}^{eff}(t) = e\frac{dx(t)}{dt} N_{C_{60}} = I_{Rb^+} \cdot \exp\left(-\frac{I_{Rb^+}}{3eN_{C_{60}}} t\right) \quad (2)$$

Figure 4d depicts the plot of I_{Rb^+} as a function of the intercalation time t. Here, we used $\Delta G_0^{\ddagger} = 0.55$ eV, $U = 0.5$ eV, and $d = 0.65$ nm. Overall, the predicted intercalation dynamics agrees well with the experimental results. In the Supporting Information, we discuss the roles of electromigration and field-induced Rb ionization in Rb^+ intercalation.

Electron−Phonon Coupling in Rb_3C_{60} Thin Films

When intercalating Rb^+ into the C_{60} crystal, the electronic structure changes to a metal with high density of states at the Fermi level which boosts electron−phonon coupling (EPC). The EPC of Raman active Rb_3C_{60} phonons can be determined by Raman spectroscopy from the full width at half-maximum (FWHM) increase when going from C_{60} to Rb_3C_{60}. In the presence of EPC, the phonon lifetime is reduced, which leads to an increase of the FWHM in Rb_3C_{60}.[25,46,47] Therefore, measuring the increase in the Raman mode's FWHM upon changing C_{60} to Rb_3C_{60} allows one to determine the EPC constant λ_i of a particular phonon.[25,46] There are 37 Raman active phonons in C_{60},[48] and FWHM Raman analysis has been used to determine the dimensionless EPC constant λ_R[49] given by

$$\lambda_R = \sum_i \lambda_i = \sum_i \frac{d_i}{\pi N(E_F)} \frac{\Delta\Gamma_i}{\omega_i^2} \quad (3)$$

In eq 3, ω_i, d_i, and $\Delta\Gamma_i$ are the unrenormalized discrete phonon frequency, mode degeneracy, and mode broadening for the i-th mode, respectively. $N(E_F)$ is the DOS at the Fermi level, which is equal to $N(E_F) = 15$ states/eV for Rb_3C_{60}.[25] Previous works found a dominant contribution of the $H_g(2)$ phonon mode which contributes $\lambda[H_g(2)] \approx 0.2$,[25,46] and a total EPC constant for all Raman active modes $\lambda_R \approx 0.5$ was claimed for thick Rb_3C_{60} films.[25] The contributions to the FWHM of Raman modes are EPC, phonon−phonon scattering, and defect scattering. The effects of phonon−phonon scattering depend on temperature, and we find only minimal change in the FWHM of $H_g(1)$ and $H_g(2)$ phonons at 5 and 300 K. The defect scattering contribution is minimized by using phase-pure Rb_3C_{60} in our experiment. In addition to Raman spectroscopy, EPC can also be determined from $d\rho/dT$, the slope of the resistivity with temperature. This determination of EPC includes all phonons (also Raman inactive phonons) whose energy is less than $k_B \cdot T$ (T is the temperature in which the linear slope is observed and k_B the Boltzmann constant).[50,51] Thus, the higher energy optical phonons observed in Raman do not contribute to the EPC constant measured in transport. To highlight the difference to

https://doi.org/10.1021/acsnano.6c02466
ACS Nano XXXX, XXX, XXX−XXX

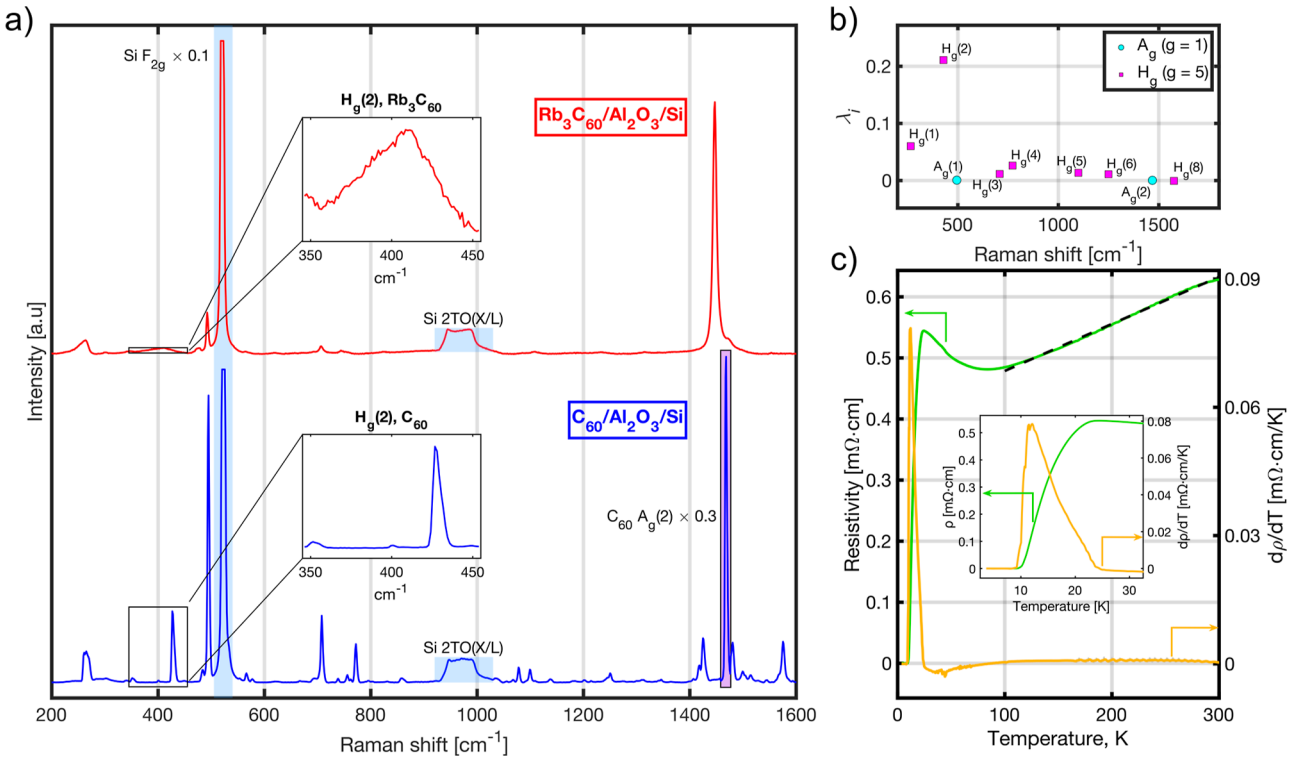

Figure 5. (a) Raman spectra of $C_{60}/Al_2O_3/Si$ and $Rb_3C_{60}/Al_2O_3/Si$. The insets show the $H_g(2)$ peaks with a large electron−phonon coupling (EPC) constant in the case of Rb_3C_{60}. The total EPC of this sample was $\lambda_R = 0.334$. (b) EPC constant of individual phonon modes versus the phonon energy. (c) Rb_3C_{60} temperature dependence of resistivity and its derivative $d\rho/dT$. In the linear regime, we obtain $d\rho/dT = 0.827$ $\mu\Omega$·cm/K yielding an EPC constant $\lambda_{tr} = 0.293$ and $T_C = 0.71$ K. The superconducting transition of this sample is characterized by $T^{zero} = 9.2$ K and $T^{onset} = 24.5$ K.

λ_R, we introduce λ_{tr}, the EPC determined from $d\rho/dT$. Previously, λ_{tr} was determined in the temperature range between 100 K and 350 K at constant volume from the measured slope $d\rho/dT$[50,51] according to

$$\lambda_{tr} = 0.246(\hbar\omega_p)^2 d\rho/dT \quad (4)$$

In eq 4, $\hbar\omega_p$ (the plasma energy) is to be taken in units of eV and $d\rho/dT$ is to be taken in units $\mu\Omega$·cm/K. The reported values for $\hbar\omega_p$ from literature have a wide range, e.g., $\hbar\omega_p$ = 0.6 eV (optical spectroscopy)[52] and $\hbar\omega_p$ = 1.2 eV (theory).[53] Using $d\rho/dT \sim 2$ $\mu\Omega$·cm/K and $\hbar\omega_p$ = 1.2 eV, $\lambda_{tr} = 0.65$ was obtained.[50] The EPC constant enters the McMillan formula for the critical temperature T_C,[54] which reads

$$T_c = \frac{\hbar\omega_{ln}}{1.2k_B}\exp\left(-\frac{1.04(1+\lambda)}{\lambda - \mu^*(1+0.62\lambda)}\right) \quad (5)$$

For Rb_3C_{60}, $\mu^* = 0.1$[22] and an average phonon frequency ω_{ln} = 1300 cm^{-1} from theory[49] have been used.[25] For $\lambda_R = 0.5$, a value of $T_C = 17$ K was predicted[25] (the actual T_C of the Rb_3C_{60} sample from transport was $T_C = 28$ K).[25] There is a discussion[26,55−58] if the McMillan formula is applicable in the case of Rb_3C_{60} because the bandwidth of the electron energy bands is close to the phonon energy and correlation effects may play a role. Usually, the inclusion of correlation effects lowers T_C, but in the case of fullerides, correlation effects and EPC can cooperate to increase T_C.[59,60] No effective theory exists that predicts T_C of Rb_3C_{60} in the presence of correlations and EPC.

Let us now determine EPC in Rb_3C_{60} from Raman and transport measurements. We have synthesized a superconducting Rb_3C_{60} film in situ and measured $\rho(T)$, from which we extracted the transition temperatures T^{zero} and T^{onset} and the slope $d\rho/dT$. We compared the observed transition temperatures to the critical temperatures estimated from EPC constants obtained from Raman and transport. Figure 5a shows Raman spectra of C_{60} and Rb_3C_{60} in the wide energy range. We employed eq 3 to determine EPC from the FWHM of each Raman active phonon mode (Figure S11). Overall, our FWHM are in good agreement to previously published works.[46,47,61] In Figure 5b, we plot the contribution of each Raman active phonon mode to the EPC constant λ_R. It can be seen that, in particular, the $H_g(2)$ phonon mode has a large contribution to the total λ_R, in agreement to previous works using Raman spectroscopy on Rb_3C_{60}[25,46,47] and a recent ARPES study on K_3C_{60}.[62] We obtain a total EPC from Raman $\lambda_R = 0.334$ from which we estimate T_C via eq 5 to obtain T_C = 0.78 K which is considerably lower than the experimental value of T_C (c.f. Figures 2f and 5c). For estimating T_C, we have used an experimental value ω_{ln} = 441 cm^{-1} which is lower than the previously used ω_{ln}.[25] We explain our lower value of ω_{ln} as follows. In the calculation of ω_{ln}, each phonon mode is weighed with its EPC constant,[49] and because of the dominance of $H_g(2)$ EPC, the resulting ω_{ln} is small in comparison to an ω_{ln} weighted by similar EPC constants. The transport EPC λ_{tr} is determined from the experimental slope whose fit is shown in Figure 5c yielding $d\rho/dT = 0.827$ $\mu\Omega$·cm/K which is a factor ∼2 lower than in previous experiments.[50] The previous experiment[50] was carried out at constant sample volume. The volume of the present thin film sample is constrained by the Si substrate with a ∼10 times lower linear thermal expansion coefficient than Rb_3C_{60}[63]

https://doi.org/10.1021/acsnano.6c02466
ACS Nano XXXX, XXX, XXX−XXX

making the present and previous experiments comparable. From $d\rho/dT$, we obtain a value of $\lambda_{tr} = 0.293$, and from eq 4, we obtain $T_C = 0.71$ K. We consider the similarity of λ_R and λ_{tr} coincidental because different phonons contribute to λ_R and λ_{tr}. We investigated the superconducting transition of the same sample used for Raman and dρ/dT measurements. Figure 5c depicts $\rho(T)$ and $d\rho/dT$ yielding $T^{onset} = 24.5$ K and $T^{zero} = 9.2$ K which is in disagreement to the estimation of T_C from λ_R and λ_{tr}. The following three points are important when discussing this disagreement. First, not all Rb_3C_{60} phonons are Raman active and λ_R and hence T_C are underestimated. Second, in λ_{tr}, only low-energy phonons contribute whose energy is below the linear $d\rho/dT$ range. The above two points explain the underestimation of T_C by considering either λ_R or λ_{tr}. It is thus likely that both λ_R and λ_{tr} contribute to the total EPC. Third, if correlation effects are present and enhance EPC,[59,60] we underestimate T_C from our EPC analysis.

CONCLUSIONS AND OUTLOOK

We have introduced electro-intercalation as a method for on-chip intercalation chemistry where ions are driven by electronic currents. Electro-intercalation can be used to control the stoichiometry in order to fine-tune phase transitions. In the present work, we have controlled the superconducting phase transition in fullerides by Rb^+ intercalation. Alkali metals with a low work function are particularly suited for electro-intercalation because the corresponding barriers for electron tunneling are small. We conclude that electro-intercalation works well for a nanostructured C_{60} film that consists of grains because such a film provides a high density of $Rb/Rb_3C_{60}/C_{60}$ interfaces. An applied current leads to a potential drop over a C_{60} grain which facilitates electron tunneling into the C_{60} grain followed by the intercalation of a Rb^+ ion. The exciting aspects of this experiment are its high level of stoichiometric precision, ultimate cleanliness ensured by UHV conditions, and spatially homogeneous doping. Moreover, there is no lower limit for the volume of the host material that can be intercalated. This doping method could also be applied to the on-chip synthesis of fulleride superconductor heterostructures. In particular, topological insulator (TI)-fulleride interfaces[9] are interesting candidates for superconducting fulleride growth on the TI and can probably be synthesized by electro-intercalation. Electro-intercalation also allows, in principle, for the synthesis of ternary fulleride superconductors such as Rb_2CsC_{60} with a higher critical temperature[24] or polymeric Mg_4C_{60}.[28] The presented experimental setup can also be used for experiments on light-induced superconductivity in Rb_3C_{60}, where the four-point resistance measurement is carried out during light irradiation. Future experiments could also include a micro-fabricated on-chip Rb or Cs ion source such as the on-chip Yb source built recently.[64] This ion source would allow for shuffling ions into the sample region. A future theoretical work could consider the unified description of processes I–III by a single theoretical method. We expect that electro-intercalation works not only in C_{60} but also in a large variety of organic materials such as picene, phenanthrene, coronene, graphene nanoribbons, and metal–organic frameworks and could be used to search for and identify new alkali metal-doped superconducting materials.

EXPERIMENTAL SECTION

Sample Preparation

In the first step (Figure 1b II), a C_{60} film was deposited on the Al_2O_3 (sapphire) substrate by evaporation from a quartz crucible resistively heated to 400 °C. The base pressure in the UHV system was $p \sim 2 \times 10^{-10}$ mbar. The deposition rate was 5 Å/min monitored and controlled using a quartz crystal microbalance (QMB). During film growth, the substrate was kept at 120 °C, followed by postannealing at 200 °C for 5 min. Hereafter, the C_{60} sample was immediately checked by Raman spectroscopy in the range of the strong $A_g(2)$ Raman mode of C_{60}, observed at 1456 cm^{-1} for C_{60} at temperatures $T > 260$ K and 1467 cm^{-1} at $T < 260$ K.

In the next step, Rb doping of C_{60} was performed by evaporation of Rb from a well-degassed getter source. The Rb flux, calibrated using a QMB, was approximately 0.1 Å/min and simultaneously monitored throughout the doping process. As the evaporation was carried out with the sample mounted on a cryomanipulator, the resistance evolution could be recorded in situ, enabling the identification of the Rb_3C_{60} phase by the characteristic resistance minimum.[40] During doping, Raman spectra were simultaneously acquired, focusing on the evolution of the $A_g(2)$ mode, which progressively shifted from the Rb_1C_{60} position at 1458 cm^{-1} toward the single Rb_3C_{60} peak at 1449 cm^{-1}. The doping was continued until the spectrum exhibited only the Rb_3C_{60} feature, indicating completion of the intercalation process. In order to resolve these peaks, all these Raman acquisitions were performed at temperatures less than 10 K.

Raman Spectroscopy and Mapping

Raman spectroscopy was performed using $\lambda_{ext} = 532$ nm excitation wavelength with a laser power $P \approx 10$ mW. The cryomanipulator in our experimental setup was equipped with two encoded stepper motors. It allowed automated sample translations in the plane perpendicular to the laser beam. The minimal stepsize for translation was 250 nm. The mapping spatial resolution was limited by the laser beam spotsize arising from excitation wavelength λ_{ext} and numerical aperture NA of the objective, which in our case was estimated from the Airy pattern diameter as follows: $d \approx 1.22\lambda_{ext}/NA \approx 1.18$ μm.

Electrical Transport Characterization

Electrical transport measurements were performed in a van der Pauw geometry with electrical contacts precisely placed at the four corners of squared substrate. The temperature-dependent resistivity and superconducting transition were measured with a precision current source Keithley 6220 and nanovoltmeter Keithley 2182A operated in Delta mode to suppress spurious thermoelectric voltages. The Delta acquisition frequency was set at 1 Hz, and the magnitude of the excitation current was 1 μA, ensuring negligible self-heating of the sample in the superconducting state.

During the electro-intercalation process, the sample resistance was continuously monitored using a Sourcemeter Keithley 2400 operating in a DC mode with a constant current of 10 μA, while the voltage drop across the film was recorded simultaneously. Electrical transport measurements also allow for the verification of the film homogeneity by interchanging the current and voltage contact pairs and by rotating the measurement configuration by 90°, as permitted by the van der Pauw geometry. Considering the strict square substrate geometry and the accurate placement of the contacts in the corners, the variation in the measured resistances of all configurations did not exceed 5%.

Rb_xC_{60} Stoichiometry Estimation Using Raman Spectra

We determine the Rb_xC_{60} stoichiometry from the $A_g(2)$ Raman peak components corresponding to C_{60}, Rb_1C_{60}, and Rb_3C_{60}. For the analysis, we assume that the number of C_{60} molecules inside the laser spot is conserved during Rb intercalation. The peak areas of components C_{60}, Rb_1C_{60}, and Rb_3C_{60} in the i-th doping step are denoted by $A_i^{C_{60}}$, $A_i^{Rb_1C_{60}}$, and $A_i^{Rb_3C_{60}}$, respectively. Then x_i, the stoichiometry in the i-th doping step, is given by

https://doi.org/10.1021/acsnano.6c02466
ACS Nano XXXX, XXX, XXX–XXX

$$x_i = \alpha \cdot \frac{A_i^{Rb_1C_{60}}}{A_0^{C_{60}}} + 3\beta \cdot \frac{A_i^{Rb_3C_{60}}}{A_0^{C_{60}}} \quad (6)$$

The parameters α and β are determined from a regression analysis as $\alpha = 5.84$ and $\beta = 2.95$, respectively (Supporting Information). The relative Raman cross sections for C_{60}, Rb_1C_{60}, and Rb_3C_{60} are equal to 1, $1/\alpha$, and $1/\beta$, respectively. Let us consider a general sample which has three Raman peaks and consists of C_{60}, Rb_1C_{60}, and Rb_3C_{60} fractions with relative Raman cross sections of 1, 0.17, and 0.34, respectively. We assume that the error bar of the Raman peak corresponding to each phase is given by the noise of the Raman spectrum. From the experimentally observed noise, we estimate at most 10% error for the Raman intensities (see Figure 2f). Considering a stoichiometry x close to $x = 3$, we typically have an intense Raman peak corresponding to Rb_3C_{60} and a weaker or no Raman peak corresponding to C_{60}. The cross section of C_{60} is ~3 times higher than the cross section of Rb_3C_{60}. Therefore, if we have a Rb_3C_{60} sample and see no C_{60} peak, it means the error bar of the stoichiometry $x = 3$ is about $10\%/3 \approx 3\%$. For mixed phases, the error can be slightly higher because of the contributions of all three peaks to the total error.

Quantum-Chemical Calculations

Density functional theory (DFT) calculations were performed using the Vienna Ab initio Simulation Package (VASP) version 6.4.2.[65,66] Interactions between ion cores and valence electrons were treated using the projector-augmented wave (PAW) method.[67,68] Exchange–correlation effects were described using the Perdew–Burke–Ernzerhof (PBE) generalized gradient approximation (GGA) functional.[69] The Rb_{sv} PAW potential with a valence electron configuration of $4s^24p^65s^1$ and the standard C PAW potential with a valence electron configuration of $2s^22p^2$ were used. A plane-wave energy cutoff of 500 eV and a 2×2×2 Monkhorst–Pack k-point mesh were applied. Structural relaxations were converged to 10^{-5} eV in total energy and 0.01 eV·Å^{-1} in forces. Reference structures for pristine C_{60} and fully intercalated Rb_3C_{60} were obtained by relaxing the $Fm\bar{3}m$ cubic phase. The optimized lattice constant was 14.797 Å for C_{60} and 15.104 Å for Rb_3C_{60} (~2% expansion upon intercalation). Using the relaxed Rb_3C_{60} structure, minimum-energy migration pathways for isolated Rb^+ hopping and vacancy migration between the octahedral (O_h) and tetrahedral (T_d) pockets were calculated with the climbing-image nudged elastic band (CI-NEB) method,[70] thereby providing the bulk migration barriers. To investigate Rb transport across the Rb–C_{60} interface, slab supercells were constructed containing a Rb slab in contact with two C_{60} layers. Three interface geometries were considered, including vdW-vdW, vdW-10 Å, and vdW-20 Å, to compare the Rb migration at vdW-sized and large imposed interfacial gaps. Two other interface geometries, 10 Å-10 Å and 20 Å-20 Å, were also constructed to determine the energy barrier for Rb migration across the 10 Å and 20 Å interfacial gaps. The in-plane lattice constants were fixed to those of the relaxed Rb^+ structure, and a sufficiently large out-of-plane cell dimension was used to preserve the intended gap sizes. During relaxation, the middle layer of the Rb slab was held fixed to mimic bulk-like behavior of the Rb nanowire. All numerical settings for the slab calculations were identical to those used for the bulk systems, except that a Γ-centered 4 × 4 × 1 k-point mesh was employed and a 0.02 eV·Å^{-1} force tolerance was used during relaxations and CI-NEB calculations. CI-NEB was then applied to obtain minimum-energy paths and transition states (TS) for Rb migration across various interfacial gaps. Bader charge analysis[71] was used to quantify the charge state of the migrating Rb atom along each CI-NEB pathway.

Estimate of the Rb^+ Diffusion Coefficient and Intercalation Time

To obtain a realistic estimate of the Rb^+ diffusion prefactor and diffusion coefficient in the Rb-rich lattice, we complemented the DFT CI-NEB barriers with finite-temperature molecular dynamics using Grimme's extended tight-binding (xTB) Hamiltonian,[72,73] as implemented in the DFTB+ code.[74,75] The Rb_3C_{60} $Fm\bar{3}m$ structure (four C_{60} and 12 Rb per cell) was first reoptimized at the xTB level, and NVT dynamics at $T = 300$ K were carried out with a Nose–Hoover thermostat for 5 ps simulation time and using a 1 fs time step. Selected Rb ions that remained localized in either O_h or T_d sites were monitored and their velocities projected onto the geometric hop direction between neighboring O_h and T_d pockets. From the velocity autocorrelation function and its Fourier transform, we extracted characteristic vibrational frequencies along the hop direction and, by multiplying with the coordination numbers of the corresponding sites, effective attempt frequencies.

■ ASSOCIATED CONTENT

Supporting Information

The Supporting Information is available free of charge at https://pubs.acs.org/doi/10.1021/acsnano.6c02466.

Photograph of the sample inside UHV through the inverted flange; regression analysis for stoichiometry determination by Raman spectroscopy; individual Raman spectra of Raman maps; line shape analysis for stoichiometry determination; thickness-dependent conductivity for a 12 and 30 nm Rb_3C_{60} film; resistance of the residual Rb channels; stoichiometry determination and $\rho(T)$ for each stoichiometry x; calculation of the vdW intercalation barrier; Bader charge analysis; calculation of the diffusion barrier for Rb inside C_{60}; calculation of intercalation time; details for the Butler–Volmer model; calculation of the tunneling barrier between Rb and Rb_3C_{60}; and determination of FWHM of Raman modes in C_{60} and Rb_3C_{60} (PDF)

■ AUTHOR INFORMATION

Corresponding Authors

Konstantin P. Shchukin – *Institut für Festkörperelektronik, Technische Universität Wien, Vienna 1040, Austria; II. Physikalisches Institut, Universität zu Köln, Cologne 50937, Germany;* orcid.org/0000-0003-4766-427X; Email: konstantin.shchukin@tuwien.ac.at

Alexander Grüneis – *Institut für Festkörperelektronik, Technische Universität Wien, Vienna 1040, Austria;* orcid.org/0000-0003-2448-6060; Email: alexander.grueneis@tuwien.ac.at

Authors

Oliver N. Gallego Lacey – *CEA, Universite Grenoble Alpes, Grenoble 38000, France*

Baptiste Coquinot – *Institute of Science and Technology Austria (ISTA), Klosterneuburg 3400, Austria*

Jacek Jakowski – *Computational Sciences & Engineering Division, Oak Ridge National Laboratory, Oak Ridge, Tennessee 37831, United States;* orcid.org/0000-0003-4906-3574

Jingsong Huang – *Center for Nanophase Materials Sciences, Oak Ridge National Laboratory, Oak Ridge, Tennessee 37831, United States;* orcid.org/0000-0001-8993-2506

Patrik Staudenmayer – *Institut für Festkörperelektronik, Technische Universität Wien, Vienna 1040, Austria*

Yannic Falke – *II. Physikalisches Institut, Universität zu Köln, Cologne 50937, Germany*

Ram Prakash Pandeya – *Institut für Festkörperelektronik, Technische Universität Wien, Vienna 1040, Austria*

Complete contact information is available at: https://pubs.acs.org/10.1021/acsnano.6c02466

https://doi.org/10.1021/acsnano.6c02466
ACS Nano XXXX, XXX, XXX–XXX

Funding

The authors acknowledge TU Wien Bibliothek for financial support through its Open access funding provided by Technische Universitat Wien.

Notes

This manuscript has been authored by UT-Battelle, LLC, under contract DE-AC05-00OR22725 with the U.S. Department of Energy. The publisher acknowledges the U.S. Government license to provide public access under the DOE Public Access Plan.
The authors declare no competing financial interest.

■ ACKNOWLEDGMENTS

A.G. and K.P.S. acknowledge the DFG through CRC 1238 (277146847, A01) and DFG project SE 2575. K.P.S., P.S., and A.G. would like to thank the Center for Micro- and Nanostructures (ZMNS) for providing the cleanroom facilities. K.P.S. thanks Daniele Nazari for help with ALD of Al_2O_3 films. Financial support from FFG Austria (CrystalGate) is acknowledged. A.G. thanks John Weaver for discussions about the structure of Rb_xC_{60}. B.C. acknowledges support from the NOMIS Foundation. First-principles simulations were supported as part of user project CNMS2025-R-03182 at the Center for Nanophase Materials Sciences (CNMS), which is a US Department of Energy, Office of Science User Facility at Oak Ridge National Laboratory. J.J. and J.H. acknowledge the computational resources provided by the ACCESS (Advanced Cyberinfrastructure Coordination Ecosystem: Services & Support) program through allocation TG-DMR110037; the National Energy Research Scientific Computing Center (NERSC), a DOE Office of Science User Facility supported under Contract No. DE-AC02-05CH11231, through NERSC award BES-ERCAP0031261; and the Compute and Data Environment for Science (CADES) Baseline at Oak Ridge National Laboratory, supported by the Office of Science of the U.S. Department of Energy under Contract No. DE-AC05-00OR22725.

■ REFERENCES

(1) Haddon, R. C.; Hebard, A. F.; Rosseinsky, M. J.; Murphy, D. W.; Duclos, S. J.; Lyons, K. B.; Miller, B.; Rosamilia, J. M.; Fleming, R. M.; Kortan, A. R.; Glarum, S. H.; Makhija, A. V.; Muller, A. J.; Eick, R. H.; Zahurak, S. M.; Tycko, R.; Dabbagh, G.; Thiel, F. A. Conducting films of C_{60} and C_{70} by alkali-metal doping. *Nature* **1991**, *350*, 320−322.
(2) Wang, M.; Kumar, A.; Dong, H.; Woods, J. M.; Pondick, J. V.; Xu, S.; Hynek, D. J.; Guo, P.; Qiu, D. Y.; Cha, J. J. A Gapped Phase in Semimetallic T_d-WTe_2 Induced by Lithium Intercalation. *Adv. Mater.* **2022**, *34*, 2209397.
(3) Bediako, D. K.; Rezaee, M.; Yoo, H.; Larson, D. T.; Zhao, S. F.; Taniguchi, T.; Watanabe, K.; Brower-Thomas, T. L.; Kaxiras, E.; Kim, P. Heterointerface effects in the electrointercalation of van der Waals heterostructures. *Nature* **2018**, *558*, 425−429.
(4) Ro, Y. G.; Na, S.; Kim, J.; Chang, Y.; Lee, S.; Kwak, M. S.; Jung, S.; Ko, H. Iontronics: Neuromorphic Sensing and Energy Harvesting. *ACS Nano* **2025**, *19*, 24425−24507.
(5) Robin, P.; Kavokine, N.; Bocquet, L. Modeling of emergent memory and voltage spiking in ionic transport through angstrom-scale slits. *Science* **2021**, *373*, 687−691.
(6) Wang, H.; Wang, J.; Li, W.; Hu, J.; Dong, J.; Zhai, D.; Kang, F. Stable Cycling of Na Metal Batteries at Ultrahigh Capacity. *Adv. Mater.* **2024**, *36*, 2409062.
(7) Sau, K.; Takagi, S.; Ikeshoji, T.; Kisu, K.; Sato, R.; dos Santos, E. C.; Li, H.; Mohtadi, R.; Orimo, S.-i. Unlocking the secrets of ideal fast ion conductors for all-solid-state batteries. *Commun. Mater.* **2024**, *5*, 122.
(8) Mitrano, M.; Cantaluppi, A.; Nicoletti, D.; Kaiser, S.; Perucchi, A.; Lupi, S.; Di Pietro, P.; Pontiroli, D.; Ricco, M.; Clark, S. R.; et al. Possible light-induced superconductivity in K_3C_{60} at high temperature. *Nature* **2016**, *530*, 461−464.
(9) Pandeya, R. P.; Shchukin, K. P.; Falke, Y.; Mussler, G.; Jalil, A. R.; Atodiresei, N.; Hasdeo, E. H.; Fedorov, A.; Senkovskiy, B. V.; Jansen, D.; Di Santo, G.; Petaccia, L.; Grüneis, A. Molecular Order Induced Charge Transfer in a C_{60}-Topological Insulator Moire Heterostructure. *Nano Lett.* **2025**, *25*, 1220−1225.
(10) Fleming, R. M.; Ramirez, A. P.; Rosseinsky, M. J.; Murphy, D. W.; Haddon, R. C.; Zahurak, S. M.; Makhija, A. V. Relation of structure and superconducting transition temperatures in A_3C_{60}. *Nature* **1991**, *352*, 787−788.
(11) Rosseinsky, M. J.; Ramirez, A. P.; Glarum, S. H.; Murphy, D. W.; Haddon, R. C.; Hebard, A. F.; Palstra, T. T. M.; Kortan, A. R.; Zahurak, S. M.; Makhija, A. V. Superconductivity at 28 K in Rb_xC_{60}. *Phys. Rev. Lett.* **1991**, *66*, 2830−2832.
(12) Hebard, A. F.; Rosseinsky, M. J.; Haddon, R. C.; Murphy, D. W.; Glarum, S. H.; Palstra, T. T. M.; Ramirez, A. P.; Kortan, A. R. Superconductivity at 18 K in potassium-doped C_{60}. *Nature* **1991**, *350*, 600−601.
(13) Stepniak, F.; Benning, P. J.; Poirier, D. M.; Weaver, J. H. Electrical transport in Na, K, Rb, and Cs fullerides: Phase formation, microstructure, and metallicity. *Phys. Rev. B* **1993**, *48*, 1899−1906.
(14) Poirier, D.; Ohno, T.; Kroll, G.; Benning, P.; Stepniak, F.; Weaver, J.; Chibante, L.; Smalley, R. X-ray photoemission investigations of binary and ternary C_{60} fullerides of Na, K, Rb, and Cs. *Phys. Rev. B* **1993**, *47*, 9870.
(15) Buffinger, D. R.; Ziebarth, R. P.; Stenger, V. A.; Recchia, C.; Pennington, C. H. Rapid and efficient synthesis of alkali metal-C_{60} compounds in liquid ammonia. *J. Am. Chem. Soc.* **1993**, *115*, 9267−9270.
(16) Yoon, T.; Koo, J. Y.; Choi, H. C. High Yield Organic Superconductors via Solution-Phase Alkali Metal Doping at Room Temperature. *Nano Lett.* **2020**, *20*, 612−617.
(17) Dalchiele, E.; Rosolen, J. M.; Decker, F. Electrochemically intercalated M_xC_{60} thin films in a solid state cell (M = Li, K): Optical and photoelectrochemical characterization. *Appl. Phys. A: Mater. Sci. Process.* **1996**, *63*, 487−494.
(18) Hesper, R.; Tjeng, L. H.; Heeres, A.; Sawatzky, G. A. Photoemission evidence of electronic stabilization of polar surfaces in K_3C_{60}. *Phys. Rev. B* **2000**, *62*, 16046−16055.
(19) Rogge, S.; Durkut, M.; Klapwijk, T. M. Single domain transport measurements of C_{60} films. *Phys. Rev. B* **2003**, *67*, 033410.
(20) Palstra, T.; Hebard, A.; Haddon, R.; Littlewood, P. Fermi-liquid behavior in the electrical resistivity of K_3C_{60} and Rb_3C_{60}. *Phys. Rev. B* **1994**, *50*, 3462.
(21) Broussely, M.; Biensan, P.; Bonhomme, F.; Blanchard, P.; Herreyre, S.; Nechev, K.; Staniewicz, R. J. Main aging mechanisms in Li ion batteries. *J. Power Sources* **2005**, *146*, 90−96.
(22) Schluter, M.; Lannoo, M.; Needels, M.; Baraff, G. A.; Tomanek, D. Electron-phonon coupling and superconductivity in alkali-intercalated C_{60} solid. *Phys. Rev. Lett.* **1992**, *68*, 526−529.
(23) Jishi, R. A.; Dresselhaus, M. S. Electron-phonon coupling strength and implications for superconductivity in alkali-metal-doped fullerenes. *Phys. Rev. B* **1992**, *45*, 2597−2600.
(24) Takabayashi, Y.; Prassides, K. *Struct. Bonding (Berlin)*; Springer, 2016; Vol. *172*, pp 119−138.
(25) Zhou, P.; Wang, K.-A.; Eklund, P. C.; Dresselhaus, G.; Dresselhaus, M. S. Raman-scattering study of the electron-phonon interaction in M_3C_{60} (M = K,Rb). *Phys. Rev. B* **1993**, *48*, 8412−8417.
(26) Chakravarty, S.; Gelfand, M. P.; Kivelson, S. Electronic correlation effects and superconductivity in doped fullerenes. *Science* **1991**, *254*, 970−974.
(27) Kasahara, Y.; Takeuchi, Y.; Zadik, R. H.; Takabayashi, Y.; Colman, R. H.; McDonald, R. D.; Rosseinsky, M. J.; Prassides, K.;

https://doi.org/10.1021/acsnano.6c02466
ACS Nano XXXX, XXX, XXX−XXX

Iwasa, Y. Upper critical field reaches 90 Tesla near the Mott transition in fulleride superconductors. *Nat. Commun.* **2017**, *8*, 14467.
(28) Meirzadeh, E.; Evans, A. M.; Rezaee, M.; Milich, M.; Dionne, C. J.; Darlington, T. P.; Bao, S. T.; Bartholomew, A. K.; Handa, T.; Rizzo, D. J.; Wiscons, R. A.; Reza, M.; Zangiabadi, A.; Fardian-Melamed, N.; Crowther, A. C.; Schuck, P. J.; Basov, D. N.; Zhu, X.; Giri, A.; Hopkins, P. E.; et al. A few-layer covalent network of fullerenes. *Nature* **2023**, *613*, 71−76.
(29) Senkovskiy, B. V.; Nenashev, A. V.; Alavi, S. K.; Falke, Y.; Hell, M.; Bampoulis, P.; Rybkovskiy, D. V.; Usachov, D. Y.; Fedorov, A. V.; Chernov, A. I.; Gebhard, F.; Meerholz, K.; Hertel, D.; Arita, M.; Okuda, T.; Miyamoto, K.; Shimada, K.; Fischer, F. R.; Michely, T.; Baranovskii, S. D.; et al. Tunneling current modulation in atomically precise graphene nanoribbon heterojunctions. *Nat. Commun.* **2021**, *12*, 2542.
(30) Shchukin, K. P.; Hell, M.; Grüneis, A. Combined Raman spectroscopy and electrical transport measurements in ultra-high vacuum down to 3.7 K. *Rev. Sci. Instrum.* **2024**, *95*, 123901.
(31) van der Pauw, L. J. A method of measuring the resistivity and Hall coefficient on lamellae of arbitrary shape. *Philips Technol. Rev.* **1958**, *20*, 220−224.
(32) Winter, J.; Kuzmany, H. Potassium-doped fullerene K_xC_{60} with x = 0, 1, 2, 3, 4, and 6. *Solid State Commun.* **1992**, *84*, 935−938.
(33) Palstra, T. T. M.; Haddon, R. C.; Hebard, A. F.; Zaanen, J. Electronic transport properties of K_3C_{60} films. *Phys. Rev. Lett.* **1992**, *68*, 1054−1057.
(34) Amelines-Sarria, O.; dos Santos Claro, P. C.; Schilardi, P. L.; Blum, B.; Rubert, A.; Benitez, G.; Basiuk, V. A.; González Orive, A.; Hernández Creus, A.; Díaz, C.; et al. Electronic and magnetic properties of C_{60} thin films under ambient conditions: A multi-technique study. *Org. Electron.* **2011**, *12*, 1483−1492.
(35) Stankowski, J.; Kevan, L.; Czyzak, B.; Andrzejewski, B. A model for rubidium diffusion in Rb_xC_{60} fullerites. *J. Phys. Chem.* **1993**, *97*, 10430−10432.
(36) Sannicolo, T.; Charvin, N.; Flandin, L.; Kraus, S.; Papanastasiou, D. T.; Celle, C.; Simonato, J.-P.; Munoz-Rojas, D.; Jiménez, C.; Bellet, D. Electrical mapping of silver nanowire networks: a versatile tool for imaging network homogeneity and degradation dynamics during failure. *ACS Nano* **2018**, *12*, 4648−4659.
(37) Aslamasov, L.; Larkin, A. The influence of fluctuation pairing of electrons on the conductivity of normal metal. *Phys. Lett. A* **1968**, *26*, 238−239.
(38) Berezinskii, V. Destruction of long-range order in one-dimensional and two-dimensional systems possessing a continuous symmetry group. II. Quantum systems. *Sov. Phys. JETP* **1972**, *34*, 1144−1156.
(39) Kosterlitz, J. M.; Thouless, D. J. Ordering, metastability and phase transitions in two-dimensional systems. *J. Phys. C: Solid State Phys.* **1973**, *6*, 1181.
(40) Haddon, R.; Perel, A.; Morris, R.; Chang, S.-H.; Fiory, A.; Hebard, A.; Palstra, T.; Kochanski, G. Electrical resistivity and stoichiometry of K_xC_{60}, Rb_xC_{60}, and Cs_xC_{60} films. *Chem. Phys. Lett.* **1994**, *218*, 100−106.
(41) Callaway, J.; Morgan, D. F., Jr Cohesive Energy and Wave Functions for Rubidium. *Phys. Rev.* **1958**, *112*, 334.
(42) Zhang, Z.; Yates Jr, J. T. Band bending in semiconductors: chemical and physical consequences at surfaces and interfaces. *Chem. Rev.* **2012**, *112*, 5520−5551.
(43) Hall, T.; Mee, C. The work function of rubidium. *Phys. Status Solidi A* **1974**, *21*, 109−113.
(44) Lof, R.; van Veenendaal, M. v.; Koopmans, B.; Jonkman, H.; Sawatzky, G. Band gap, excitons, and Coulomb interaction in solid C_{60}. *Phys. Rev. Lett.* **1992**, *68*, 3924.
(45) Kang, S.; Yi, Y.; Kim, C.; Whang, C. Electronic Structure of C_{60} on Au Studied by Using X-ray and UV Photoelectron Spectroscopy. *J. Korean Phys. Soc.* **2005**, *46*, 1148−1151.
(46) Mitch, M. G.; Chase, S. J.; Lannin, J. S. Raman scattering and electron-phonon coupling in Rb_xC_{60}. *Phys. Rev. Lett.* **1992**, *68*, 883−886.
(47) Kelly, M. K.; Thomsen, C. Excitation energy and temperature-dependent Raman study of Rb_3C_{60} films. *Phys. Rev. B* **1994**, *50*, 18572−18579.
(48) Kuzmany, H.; Pfeiffer, R.; Hulman, M.; Kramberger, C. Raman spectroscopy of fullerenes and fullerene−nanotube composites. *Philos. Trans. R. Soc., A* **2004**, *362*, 2375−2406.
(49) Schlüter, M.; Lannoo, M.; Needels, M.; Baraff, G.; Tomanek, D. Superconductivity in alkali intercalated C_{60}. *J. Phys. Chem. Solids* **1992**, *53*, 1473−1485.
(50) Vareka, W. A.; Zettl, A. Linear Temperature Dependent Resistivity at Constant Volume in Rb_3C_{60}. *Phys. Rev. Lett.* **1994**, *72*, 4121−4124.
(51) Vareka, W.; Fuhrer, M.; Zettl, A. Temperature dependent resistivity in Rb_3C_{60}: constant volume versus constant pressure. *Phys. C (Amsterdam, Neth.)* **1994**, *235*, 2507−2508.
(52) Degiorgi, L.; Nicol, E.; Klein, O.; Grüner, G.; Wachter, P.; Huang, S.-M.; Wiley, J.; Kaner, R. Optical properties of the alkali-metal-doped superconducting fullerenes: K_3C_{60} and Rb_3C_{60}. *Phys. Rev. B* **1994**, *49*, 7012.
(53) Gunnarsson, O.; Han, J. E. The mean free path for electron conduction in metallic fullerenes. *Nature* **2000**, *405*, 1027−1030.
(54) McMillan, W. Transition temperature of strong-coupled superconductors. *Phys. Rev.* **1968**, *167*, 331.
(55) Chakravarty, S.; Khlebnikov, S.; Kivelson, S. Comment on Electron-phonon coupling and superconductivity in alkali-intercalated C_{60} solid. *Phys. Rev. Lett.* **1992**, *69*, 212.
(56) Cappelluti, E.; Grimaldi, C.; Pietronero, L.; Strässler, S.; Ummarino, G. A. Superconductivity of Rb_3C_{60}: breakdown of the Migdal-Eliashberg theory. *Eur. Phys. J. B* **2001**, *21*, 383−391.
(57) Grimaldi, C.; Cappelluti, E.; Pietronero, L.; Strässler, S. Nonadiabatic superconductivity in fullerene-based materials. *Phys. Solid State* **2002**, *44*, 454−458.
(58) Han, J. E.; Gunnarsson, O.; Crespi, V. H. Strong Superconductivity with Local Jahn-Teller Phonons in C_{60} Solids. *Phys. Rev. Lett.* **2003**, *90*, 167006.
(59) Capone, M.; Fabrizio, M.; Castellani, C.; Tosatti, E. Strongly Correlated Superconductivity. *Science* **2002**, *296*, 2364−2366.
(60) Yamazaki, S.; Kuramoto, Y. Cooperation between Coulomb and Electron-Phonon Interactions in Fulleride Superconductors. *JPS Conference Proceedings*, 2014.
(61) Mitch, M. G.; Chase, S. J.; Lannin, J. S. Variations of electron-phonon coupling in alkali-metal−C_{60} solid solutions. *Phys. Rev. B* **1992**, *46*, 3696−3699.
(62) Zhou, J. S.; Xu, R. Z.; Yu, X. Q.; Cheng, F. J.; Zhao, W. X.; Du, X.; Wang, S. Z.; Zhang, Q. Q.; Gu, X.; He, S. M.; Li, Y. D.; Ren, M. Q.; Ma, X. C.; Xue, Q. K.; Chen, Y. L.; Song, C. L.; Yang, L. X. Evidence for Band Renormalizations in Strong-Coupling Superconducting Alkali-Fulleride Films. *Phys. Rev. Lett.* **2023**, *130*, 216004.
(63) Burkhart, G. J.; Meingast, C. High-resolution thermal expansion of superconducting fullerides A_3C_{60}(A = K,Rb). *Phys. Rev. B* **1996**, *54*, R6865−R6868.
(64) Kumar, V.; Siegele-Brown, M.; Rahimi, P.; Aylett, M.; Weidt, S.; Hensinger, W. K. Fast-response low-power atomic oven for integration into an ion microchip. *Appl. Phys. Lett.* **2025**, *126*, 264001.
(65) Kresse, G.; Hafner, J. Ab initio molecular dynamics for liquid metals. *Phys. Rev. B* **1993**, *47*, 558−561.
(66) Kresse, G.; Furthmüller, J. Efficient iterative schemes for ab initio total-energy calculations using a plane-wave basis set. *Phys. Rev. B* **1996**, *54*, 11169−11186.
(67) Blöchl, P. E. Projector augmented-wave method. *Phys. Rev. B* **1994**, *50*, 17953−17979.
(68) Kresse, G.; Joubert, D. From ultrasoft pseudopotentials to the projector augmented-wave method. *Phys. Rev. B* **1999**, *59*, 1758−1775.
(69) Perdew, J. P.; Burke, K.; Ernzerhof, M. Generalized Gradient Approximation Made Simple. *Phys. Rev. Lett.* **1996**, *77*, 3865−3868.
(70) Henkelman, G.; Uberuaga, B. P.; Jonsson, H. A climbing image nudged elastic band method for finding saddle points and minimum energy paths. *J. Chem. Phys.* **2000**, *113*, 9901−9904.

https://doi.org/10.1021/acsnano.6c02466
ACS Nano XXXX, XXX, XXX−XXX

(71) Tang, W.; Sanville, E.; Henkelman, G. A grid-based Bader analysis algorithm without lattice bias. *J. Phys.: Condens. Matter* **2009**, *21*, 084204.
(72) Grimme, S.; Antony, J.; Ehrlich, S.; Krieg, H. A consistent and accurate ab initio parametrization of density functional dispersion correction (DFT-D) for the 94 elements H-Pu. *J. Chem. Phys.* **2010**, *132*, 154104.
(73) Grimme, S.; Ehrlich, S.; Goerigk, L. Effect of the damping function in dispersion corrected density functional theory. *J. Comput. Chem.* **2011**, *32*, 1456−1465.
(74) Hourahine, B.; Berdakin, M.; Bich, J. A.; Bonafe, F. P.; Camacho, C.; Cui, Q.; Deshaye, M. Y.; Diaz Miron, G.; Ehlert, S.; Elstner, M.; Frauenheim, T.; Goldman, N.; Gonzalez Leon, R. A.; van der Heide, T.; Irle, S.; Kowalczyk, T.; Kubar, T.; Lee, I. S.; Lien-Medrano, C. R.; Maryewski, A.; et al. Recent Developments in DFTB +, a Software Package for Efficient Atomistic Quantum Mechanical Simulations. *J. Phys. Chem. A* **2025**, *129*, 5373−5390.
(75) Hourahine, B.; Aradi, B.; Blum, V.; Bonafe, F.; Buccheri, A.; Camacho, C.; Cevallos, C.; Deshaye, M. Y.; Dumitrica, T.; Dominguez, A.; Ehlert, S.; Elstner, M.; van der Heide, T.; Hermann, J.; Irle, S.; Kranz, J. J.; Köhler, C.; Kowalczyk, T.; Kubar, T.; Lee, I. S.; et al. DFTB+, a software package for efficient approximate density functional theory based atomistic simulations. *J. Chem. Phys.* **2020**, *152*, 124101.

https://doi.org/10.1021/acsnano.6c02466
ACS Nano XXXX, XXX, XXX−XXX